Biophysical Journal, Volume *120*

Supplemental Information

Mechanics of Bacterial Interaction and Death on Nanopatterned Surfaces

Amar Velic, Jafar Hasan, Zhiyong Li, and Prasad K.D.V. Yarlagadda

Supporting Text

A. Derivation of parameters for constitutive models of envelope materials

The outer membrane was modelled as two uncoupled, isotropic continuum layers. For this configuration, two- and three-dimensional moduli are related, via thickness (t_{OM}), as follows

$$K_A = \frac{E_{OM} t_{OM}}{2(1-\nu_{OM})} \tag{S1}$$

$$K_B = \frac{E_{OM} {t_{OM}}^3}{48(1-{\nu_{OM}}^2)} \tag{S2}$$

where K_A and K_B are two-dimensional stretching and bending moduli and E_{OM} and ν_{OM} are the three-dimensional, isotropic Young's modulus and Poisson's ratio, respectively. Accordingly, Young's modulus can be expressed as

$$E_{OM} = \frac{2K_A(1-\nu_{OM})}{t_{OM}} = \frac{48K_B(1-{\nu_{OM}}^2)}{{t_{OM}}^3} \tag{S3}$$

This modulus can be used for the initial linear response of a hyperelastic neo-Hookean model. The corresponding neo-Hookean parameter C_{10} can be calculated using

$$C_{10} = \frac{E_{OM}}{4(1+\nu_{OM})} \tag{S4}$$

Combining the previous relations, it is shown that

$$C_{10} = \frac{K_A(1-\nu_{OM})}{2t_{OM}(1+\nu_{OM})} = \frac{12K_B(1-\nu_{OM})}{{t_{OM}}^3} \tag{S5}$$

Subsequently, the second neo-Hookean parameter (D_1) is given by

$$C_{10}D_1 = \frac{3(1-2\nu_{OM})}{2(1+\nu_{OM})} \tag{S6}$$

These equations enabled calculating the neo-Hookean parameters (C_{10}, D_1) from experimentally reported stretching (K_A) and bending moduli (K_B) using membrane thickness (t_{OM}) and Poisson's ratio (ν_{OM}). Thickness was taken as the head-to-head distance between hydrophilic groups, commonly reported as 4nm, or 2nm per leaflet (1). Poisson's ratio was taken as 0.485 based on a recent findings from the Deserno group indicating that a value 3% smaller than the incompressible limit (ν = 0.5) applies isotopically throughout a lipid membrane (2). To cover the broad range of moduli (K_A = 50 – 250mN/m and K_B = 1 – 20k_BT) reported for bacterial membranes and mimetic lipid systems, three different configurations were studied (Table S1).

The cell wall was approximated as transversely orthotropic due to the extension of peptides in two principal axes which effectively creates a plane of isotropy. If the coordinate system is defined such that glycans lie in the first principle axis and peptides in the second and third, the plane of isotropy is the 2-3 plane (Fig. S1). Due to the isotropy of the 2-3 plane, and the symmetry of the 1-2 and 2-3 planes, the total number of independent constants is reduced from nine to five. These are listed below,

$$\begin{aligned} E_1 &= E_G \\ E_2 &= E_3 = E_P \\ \nu_{12} &= \nu_{13} = \nu_{GP} \\ \nu_{23} &= \nu_P \\ G_{12} &= G_{13} = G_{GP} \end{aligned} \tag{S7}$$

Remaining constants can then be calculated using the following relations,

$$G_P = \frac{E_P}{2(1+\nu_P)} \quad where \;\; G_P = G_{23} \tag{S8}$$

$$\frac{\nu_{ij}}{E_i} = \frac{\nu_{ji}}{E_j} \quad where \;\; i, j \in 1,2,3 \;\; and \;\; i \neq j \tag{S9}$$

Therefore, most material constants could be inferred from the Young's moduli and Poisson's ratios parallel to the surface of the cell - that is, within the 1-2 plane – which are previously reported. Their values tend to be within the range E_G = 25-75MPa, E_P = 10-30MPa , ν_{GP} = 0.32-0.67 and ν_{PG} = 0.01-0.23 (10-14). Additionally, it can be reasonably assumed that $\nu_P \approx \nu_{GP}$. Accordingly, only the orthotropic shear modulus (G_{GP}) is unknown.

Shear moduli are not explicitly reported due to the inherent difficulty of measuring shear in addition to the various practical challenges associated with the size of bacteria. To circumvent this, approximations based on empirically derived formulas and tensor rotation were used to estimate shear moduli from known parameters. These theoretical estimations have been recently demonstrated for walnut wood which, like peptidoglycan, is a heterogeneous, cellular orthotropic material (15). Several such theoretical estimations exist, listed below as seen in Bachtiar and others (15). The first two approaches ((S10) and (S11)) utilise Hankinson's formula which involves an empirically derived constant (K = 0.2, 0.4), whilst the others ((S12) and (S13)) are more generalised.

$$\begin{gathered} G_{ij} = \left[\frac{\nu_{ji}+1}{E_i} + \frac{\nu_{ij}+1}{E_j} \right]^{-1}, \quad where \;\; i, j = 2,1 \\ G_{ij} = \left[\frac{\nu_{ji}-1}{E_i} + \frac{\nu_{ij}-1}{E_j} + \frac{8}{(1-K)(E_i+E_j)} \right]^{-1}, \quad where \;\; i, j = 3,1 \end{gathered} \tag{S10}$$

$$\begin{gathered} G_{ij} = \left[\left(1 + \frac{2}{1/\nu_{ij} + 1/\nu_{ji}} \right) \left(\frac{1}{E_i} + \frac{1}{E_j} \right) \right]^{-1}, \quad where \;\; i, j = 2,1 \\ G_{ij} = \frac{(K-1)(E_i+E_j)}{2(K-1)(\nu_{ij}+\nu_{ji})-4}, \quad where \;\; i, j = 3,1 \end{gathered} \tag{S11}$$

$$G_{ij} = \left[\frac{\nu_{ji}+1}{E_i} + \frac{\nu_{ij}+1}{E_j} \right]^{-1}, \quad where \;\; i, j \in 1,2,3 \;\; and \;\; i \neq j \tag{S12}$$

$$G_{ij} = \left[\frac{\nu_{ji}}{E_i} + \frac{\nu_{ij}}{E_j} + \frac{2}{\sqrt{E_i E_j}} \right]^{-1}, \quad where \;\; i, j \in 1,2,3 \;\; and \;\; i \neq j \tag{S13}$$

Applying the above to each envelope configuration, an estimated range for the orthotropic shear modulus (G_{GP}) was derived (Table S2). The sensitivity of results to changes in the orthotropic shear modulus over this range was evaluated and found to have no significant impact. Therefore, an average value was selected and used throughout. Similarly, out-of-plane parameters (i.e. E_3, ν_{13}, ν_{23}, G_{13} and G_{23}), which were inferred thought transverse isotropy, did not play a significant role, likely due to the relative thinness of the cell wall in Gram-negative bacteria.

B. Mesh convergence study

Mesh convergence was studied by separately adjusting the in-plane and through-thickness seeds along edges A,B,C and T which are highlighted in Figure 2. The through-thickness dimension was varied from 0.5-2nm, representing four to one elements through the thinnest layer (i.e. either membrane leaflet). The in-plane dimensions were varied, as outlined in Table S3. For each case, the maximum in-plane uniaxial strain was monitored in the cell wall, inner leaflet and outer leaflet, and plotted against node count to identify sensitivity (Fig. S2). Evidently, over the tested range, element size was already within convergence. Variation to the number of elements, both in- and out-of-plane had insignificant effect on the critical strain. This reinforces the effectiveness of incompatible mode elements, which – as seen - can give accurate results in bending with only one element (2nm) through the thickness (16). In contrast, when reduced integration elements (C3D8R) were used to model the contact region, at least four (0.5nm) or more through-thickness elements were required for convergence. To ensure a mesh independent result, element sizes used throughout the study never exceeded the tested range.

C. The role of weight

The influence of weight was studied separately in the model to gauge its significance. Given that the extent of wetting by the suspension fluid is not entirely clear, weight can factor into the interaction through a combination of self-weight (F_c), buoyancy (F_b), and the weight of the fluid column above the cell (F_f) (Table S4). For instance, if the suspension fluid immerses or wets the interaction, the weight of the cell is offset by an opposing and near-equivalent buoyancy force (case one). If the fluid does not wet the interaction, buoyancy disappears (case two) and a vacuum may even be created below the cell in which case it is forced down further by the weight of the fluid column above (case three). The last two cases may occur only on a superhydrophobic nanopattern, whereas the first may be relevant for any surface hydrophobicity.

The relevant forces were modelled by applying a pressure load to the entire bottom surface of the envelope section. This pressure load (P_{app}) represented the sum of weight-related forces distributed evenly over the cell's projected area. Mathematically,

$$P_{app} = \frac{F_g - F_b + F_f}{A_p} \tag{S14}$$

where A_p is the projected cell area, calculated for a cylindrical bacteria of length l and width w, as

$$A_p = \frac{4wl - w^2(4-\pi)}{4} \tag{S15}$$

The weight of the cell (F_g) was calculated from its volume (v), density (ρ_c) and the gravitational constant (g), as follows

$$F_g = v\rho_c g \tag{S16}$$

where,

$$v = \frac{3\pi l w^2 - \pi w^3}{12} \tag{S17}$$

The buoyancy on the cell (F_b) was calculated as above, using instead the density of the suspension fluid (ρ_f),

$$F_b = v\rho_f g \tag{S18}$$

Lastly, the weight of the fluid column (F_f) was calculated with an assumed height (h),

$$F_f = hA_p\rho_f g \tag{S19}$$

For all cases, the cell size, suspension fluid density and pillar radius were modelled as 3×1μm, 1g/cm^3 and 30nm, respectively. All other parameters were taken so as to maximise emphasis. For instance, the effects of weight are expected to scale directly with spacing, therefore the upper reported spacing value for bactericidal nanopatterns (300nm) was taken (17). The cell density was also taken as an upper reported value of 1.3g/cm^3 (18). The height of the fluid column was modelled as 10mm, which is over half the depth of the cell culture plates used in the bacterial studies. Lastly, all simulations were performed with the softest envelope configuration.

Despite these overestimations, weight did not cause deformation which could be considered significant relative to adhesion-driven deformation or the extensibility limits of the envelope (Table S4). For example, the self-weight of the cell, even when unadjusted for buoyancy (cases one and two) caused maximum envelope strains below 0.01%, several magnitudes less than

strains induced by adhesion and required for rupture (Figure 7). This result is intuitive based on the difference in magnitude between cell weight and surface interaction forces. For flat surfaces, interaction forces probed by atomic force spectroscopy are commonly on the order of hundreds of pN up to several nN, even for single cells (19, 20). For nanopatterned surfaces, precise measurements of peripheral pillar deflection have shown elevated interaction forces of at least several nN up to tens of nN (21, 22). Meanwhile, the gravitational force of a bacterial cell is at most tens of fN. And though the addition of the fluid column above the cell (case three) did elicit more noteable deformation, the inclusion of such a weight is undermined by a few critical observations. Firstly, if it is to occur, this load case requires superhydrophobicity as a starting point to expel the surrounding fluid. Many bactericidal nanopatterns, however, are not superhydrophobic or even hydrophobic (17, 24-26). Interaction through fluid, therefore, seems more universally relevant, in which case the fluid column would not act on the cell. Secondly, this case implies that the killing efficiency depends almost entirely on the height of the suspension fluid (S19), a phenomenon which has not been reported previously and seems unlikely to the best of our knowledge. Hence, though it can be found elsewhere (23), this exaggerated load case does not seem representative. Even so, the strains were still one magnitude lower than that occurring at 10mJ/m^2 of adhesion energy (i.e. ε = 3 vs 35% and ε_A = 5% vs 60%).

Taking this information together, weight-related effects have trivial influence on the killing mechanism of nanopatterned surfaces. They are therefore neglected from the analysis to reduce computational cost.

D. Estimating the work of adhesion

Interaction forces are finite ranged, and evolve with distance, as typically described by the Derjaguin–Landau–Verwey–Overbeek (DLVO) model. This model is very challenging to integrate with a highly deformable material, such as the cell envelope, particularly when involving nonlinear deformation (27). Therefore, a Griffith-style approximation was adopted in the present work whereby the work of adhesion (W) was inferred from the strain energy accumulation rate (dU/dA) of the deforming envelope, following minimisation of total potential energy (Π) with respect to contact area (A). This approach is conceptually the same to that employed by Pogodin and others (28) and Li (29).

$$\prod = U - WA \tag{S20}$$

$$\frac{d\prod}{dA} = 0 \quad \rightarrow \quad W = \frac{dU}{dA} \tag{S21}$$

Even so, mimicking a continuously evolving bond front is not straightforward. To do so, several simulations were run in which a downward pressure load was applied to the bottommost face of the outer leaflet over an area bounded by a relative radius (αr) that was increased incrementally (α= 0.3: 0.1: 2). For each application area, only the maximum converged strain energy accumulation rate was taken to infer the corresponding work of adhesion and other equilibrium values (sinking depth and uniaxial in-plane strains). This maximum was found by progressively increasing the magnitude of the pressure load at each application area. In doing so, two scenarios were encountered. When the application area was relatively large ($\alpha \geq 0.9$), the maximum strain energy accumulation rate corresponded to the last converged iteration at which the contact could be resolved by the implicit solver. For a constant application area (i.e. constant α) increasing the magnitude of the pressure load produces coincident strain-area curves (Fig. S3a). Therefore, the maximum strain energy accumulation rate was calculated between the last two converged iterations. On the other hand, when the application area was relatively small ($\alpha < 0.9$), applying a progressively larger load eventually revealed a plateau and subsequent inflection of the strain-area curve (Fig. S3b). This inflection represented a transition after which further area was gained by localised element distortion, not global shape change. Therefore, beyond the inflection point, the strain-area curve was not physically representative. In either case, to calculate the maximum strain energy accumulation rate, a high order polynomial was fitted to the data and a numerical differentiation scheme (S22) was applied between the iterations (j). To achieve a smooth numerical plot, and thus a good fitting polynomial ($R^2 \sim 1$), the mesh in the contact region needed to be very fine and a small iteration size (~0.01) was required.

$$W = \frac{dU}{dA} \approx \frac{U_j - U_{j-1}}{A_j - A_{j-1}} \tag{S22}$$

Supporting Figures and Tables

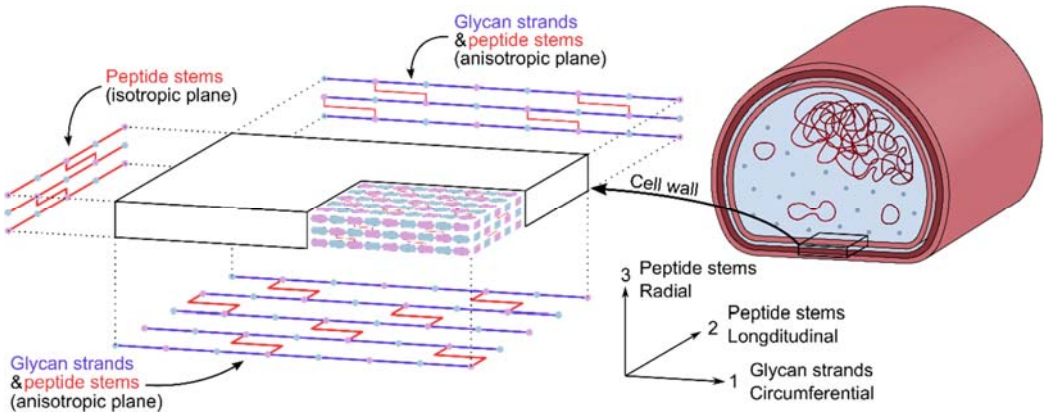

Fig. S1. Transverse isotropy of the peptidoglycan cell wall

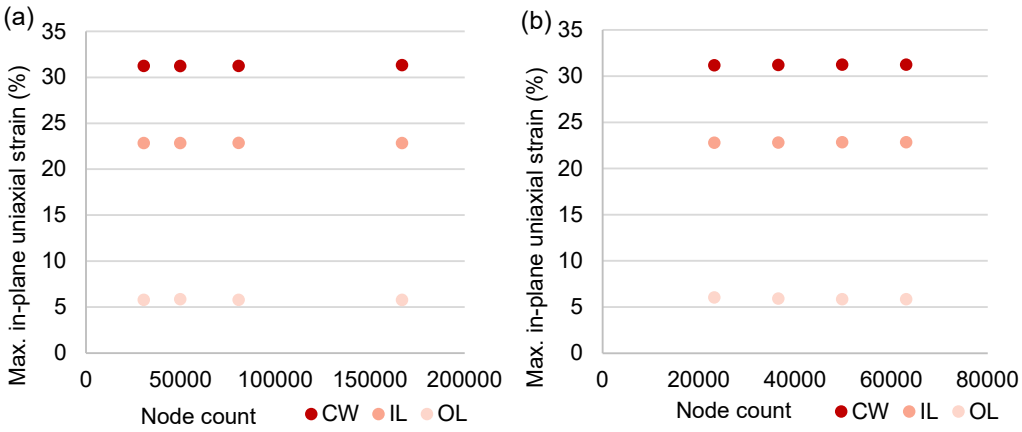

Fig. S2. Mesh convergence study. Effect of varying in-plane (a) and through-thickness (b) seeds on the maximum in-plane uniaxial strain in the cell wall (CW), inner leaflet (IL) and outer leaflet (OL).

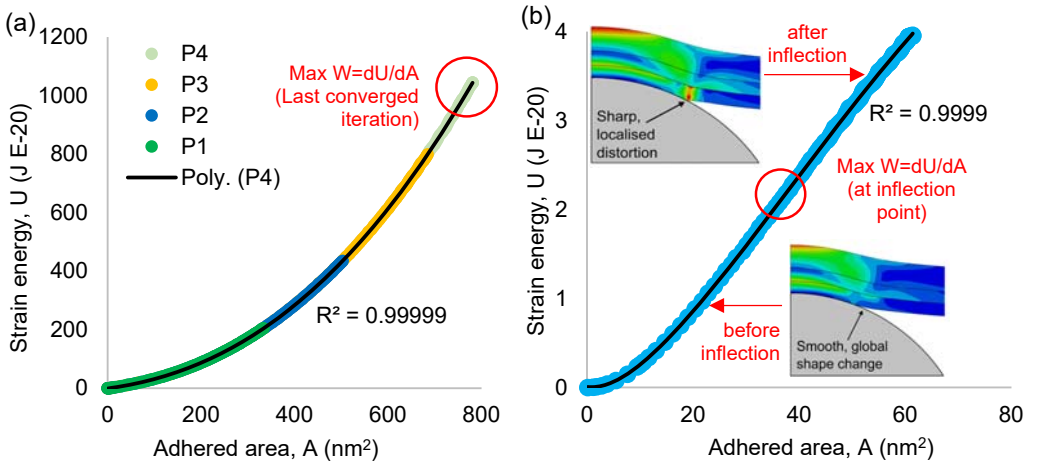

Fig. S3. Calculating the maximum work of adhesion. (a) For larger load application areas (*α≥0.9*) the maximum work of adhesion appears between the last two converged iterations. (b) For smaller areas (*α<0.9*), the maximum work of adhesion appears at an inflection point. In either case, increasing load (*P4>P3>P2>P1*) at a constant application area produces coincident strain-area curves, as seen in the left figure. R-squared values are for the fitted high order polynomial (solid black lines) used to calculate the maximum work of adhesion.

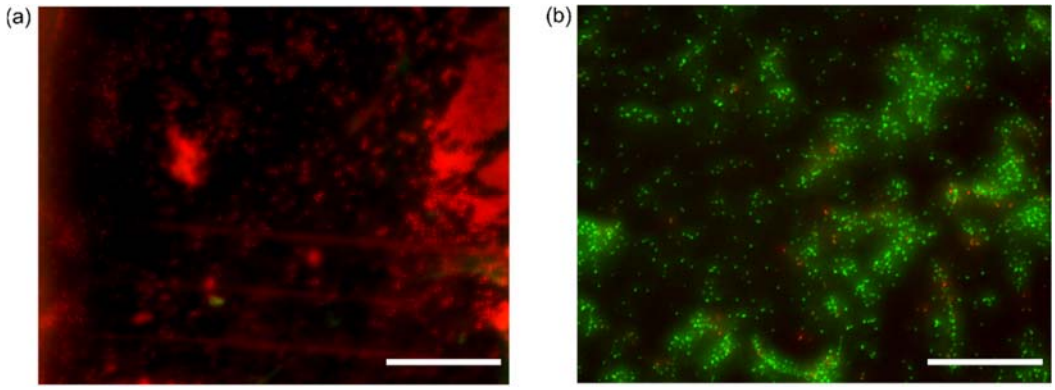

Fig. S4. Representative fluorescence microscopy images demonstrating high inactivation of *Pseudomonas aeruginosa* on cicada wing nanopatterned surface (a) in comparison to flat controls (b) after 4h incubation. Scale bars are 50μm.

Table S1. Neo-Hookean parameters used to model outer membrane

Configuration	2D moduli				neo-Hookean parameters	
	K_A (mN/m)	Ref.	K_B (k_BT)	Ref.	C_{10}	D_1
Soft	50	(3, 4)	4	(5)	1.61 MPa	0.018 MPa^{-1}
Intermediate	150	(6, 7)	12		4.83 MPa	0.006 MPa^{-1}
Stiff	250	(8, 9)	20		8.05 MPa	0.004 MPa^{-1}

Table S2. Estimation of cell wall orthotropic shear modulus

Estimation approach	Orthotropic shear modulus, G_{GP} (MPa)		
	Soft	Intermediate	Stiff
(S10)	3.55, 5.54	7.10, 11.07	10.66, 16.61
(S11)	4.58, 5.95	9.15, 11.91	13.73, 17.86
(S12)	5.54	11.07	16.61
(S13)	5.98	11.97	17.95
Selection (avg.)	5.3	10.5	15.8

Table S3. Seeding of edges for mesh convergence study

Variation	Seeds (nm)					Mesh resolution (node count)
	T	A	B	C_{min}	C_{max}	
In-plane	0.666	0.5	0.35	0.4	4	166965
	0.666	0.75	0.5	0.6	5	80685
	0.666	1	0.6	0.7	6	49800
	0.666	1.25	0.8	0.9	8	30570
Thickness	0.5	1	0.6	0.7	6	63080
	0.666	1	0.6	0.7	6	49800
	1	1	0.6	0.7	6	36520
	2	1	0.6	0.7	6	23240

Table S4. Envelope deformation due to weight

Case	Self-weight, F_g (fN)	Buoyancy, F_b (fN)	Weight of fluid column, F_c (pN)	Pressure load, P_{app} (fN/μm^2)	Max in-plane envelope strain (%)	
					ε	ε_A
1. Wetted	26.7	20.5	0	2.21	<0.01	<0.01
2. Non-wetted	26.7	0	0	9.59	<0.01	<0.01
3. Non-wetted, underlying vacuum	26.7	0	273	9.81×10^7	3	5

Supporting References

1. Shahane, G., W. Ding, M. Palaiokostas, and M. Orsi. 2019. Physical properties of model biological lipid bilayers: insights from all-atom molecular dynamics simulations. Journal of Molecular Modeling 25(3):76.
2. Terzi, M. M., M. Deserno, and J. F. Nagle. 2019. Mechanical properties of lipid bilayers: a note on the Poisson ratio. Soft Matter 15(44):9085-9092. 10.1039/C9SM01290G.
3. Nakayama, Y., K. Komazawa, N. Bavi, K.-i. Hashimoto, H. Kawasaki, and B. Martinac. 2018. Evolutionary specialization of MscCG, an MscS-like mechanosensitive channel, in amino acid transport in Corynebacterium glutamicum. Scientific Reports 8(1):12893.
4. Sun, Y., T.-L. Sun, and Huey W. Huang. 2014. Physical Properties of Escherichia coli Spheroplast Membranes. Biophysical Journal 107(9):2082-2090.
5. Deserno, M. 2007. Fluid lipid membranes–a primer.
6. Picas, L., F. Rico, and S. Scheuring. 2012. Direct measurement of the mechanical properties of lipid phases in supported bilayers. Biophysical journal 102(1):L01-L03.
7. Venable, R. M., F. L. H. Brown, and R. W. Pastor. 2015. Mechanical properties of lipid bilayers from molecular dynamics simulation. Chemistry and Physics of Lipids 192:60-74.
8. Hwang, H., N. Paracini, J. M. Parks, J. H. Lakey, and J. C. Gumbart. 2018. Distribution of mechanical stress in the Escherichia coli cell envelope. Biochimica et Biophysica Acta (BBA) - Biomembranes 1860(12):2566-2575.
9. Rawicz, W., K. C. Olbrich, T. McIntosh, D. Needham, and E. Evans. 2000. Effect of Chain Length and Unsaturation on Elasticity of Lipid Bilayers. Biophysical Journal 79(1):328-339.
10. Gumbart, J. C., M. Beeby, G. J. Jensen, and B. Roux. 2014. Escherichia coli Peptidoglycan Structure and Mechanics as Predicted by Atomic-Scale Simulations. PLOS Computational Biology 10(2):e1003475.
11. Yao, X., M. Jericho, D. Pink, and T. Beveridge. 1999. Thickness and elasticity of gram-negative murein sacculi measured by atomic force microscopy. Journal of bacteriology 181(22):6865-6875.
12. Deng, Y., M. Sun, and J. W. Shaevitz. 2011. Direct Measurement of Cell Wall Stress Stiffening and Turgor Pressure in Live Bacterial Cells. Physical Review Letters 107(15):158101.
13. Amir, A., F. Babaeipour, D. B. McIntosh, D. R. Nelson, and S. Jun. 2014. Bending forces plastically deform growing bacterial cell walls. Proceedings of the National Academy of Sciences 111(16):5778.
14. Assidi, M., F. Dos Reis, and J. F. Ganghoffer. 2011. Equivalent mechanical properties of biological membranes from lattice homogenization. Journal of the Mechanical Behavior of Biomedical Materials 4(8):1833-1845.
15. Bachtiar, E. V., M. Rüggeberg, S. Hering, M. Kaliske, and P. Niemz. 2017. Estimating shear properties of walnut wood: a combined experimental and theoretical approach. Materials and Structures 50(6):248.
16. Dassault Systèmes Simulia Corp. 2016. ABAQUS Online Documentation.
17. Modaresifar, K., S. Azizian, M. Ganjian, L. E. Fratila-Apachitei, and A. A. Zadpoor. 2019. Bactericidal effects of nanopatterns: A systematic review. Acta Biomaterialia 83:29-36.
18. Lewis, C. L., C. C. Craig, and A. G. Senecal. 2014. Mass and Density Measurements of Live and Dead Gram-Negative and Gram-Positive Bacterial Populations. 80(12):3622-3631.

19. Thwala, J. M., M. Li, M. C. Y. Wong, S. Kang, E. M. V. Hoek, and B. B. Mamba. 2013. Bacteria–Polymeric Membrane Interactions: Atomic Force Microscopy and XDLVO Predictions. Langmuir 29(45):13773-13782.

20. Harimawan, A., A. Rajasekar, and Y.-P. Ting. 2011. Bacteria attachment to surfaces – AFM force spectroscopy and physicochemical analyses. Journal of Colloid and Interface Science 364(1):213-218.

21. Oh, N., M. Jun, J. Lee, C.-Y. Eom, and S. Park. 2017. Nanomechanical Measurement of Bacterial Adhesion Force Using Soft Nanopillars. Journal of Nanoscience and Nanotechnology 17(11):7966-7970.

22. Ivanova, E. P., D. P. Linklater, M. Werner, V. A. Baulin, X. Xu, N. Vrancken, S. Rubanov, E. Hanssen, J. Wandiyanto, V. K. Truong, A. Elbourne, S. Maclaughlin, S. Juodkazis, and R. J. Crawford. 2020. The multi-faceted mechano-bactericidal mechanism of nanostructured surfaces. Proceedings of the National Academy of Sciences:201916680.

23. Mirzaali, M. J., I. C. P. v. Dongen, N. Tümer, H. Weinans, S. A. Yavari, and A. A. Zadpoor. 2018. In-silico quest for bactericidal but non-cytotoxic nanopatterns. Nanotechnology 29(43):43LT02.

24. Jaggessar, A., A. Mathew, T. Tesfamichael, H. Wang, C. Yan, and P. K. Yarlagadda. 2019. Bacteria Death and Osteoblast Metabolic Activity Correlated to Hydrothermally Synthesised TiO_2 Surface Properties. Molecules (Basel, Switzerland) 24(7):1201.

25. Michalska, M., F. Gambacorta, R. Divan, I. S. Aranson, A. Sokolov, P. Noirot, and P. D. Laible. 2018. Tuning antimicrobial properties of biomimetic nanopatterned surfaces. Nanoscale 10(14):6639-6650. 10.1039/C8NR00439K.

26. Hasan, J., Y. Xu, T. Yarlagadda, M. Schuetz, K. Spann, and P. K. D. V. Yarlagadda. 2020. Antiviral and Antibacterial Nanostructured Surfaces with Excellent Mechanical Properties for Hospital Applications. ACS Biomaterials Science & Engineering.

27. Ciavarella, M., J. Joe, A. Papangelo, and J. R. Barber. 2019. The role of adhesion in contact mechanics. Journal of The Royal Society Interface 16(151):20180738.

28. Pogodin, S., J. Hasan, Vladimir A. Baulin, Hayden K. Webb, Vi K. Truong, The H. Phong Nguyen, V. Boshkovikj, Christopher J. Fluke, Gregory S. Watson, Jolanta A. Watson, Russell J. Crawford, and Elena P. Ivanova. 2013. Biophysical Model of Bacterial Cell Interactions with Nanopatterned Cicada Wing Surfaces. Biophysical Journal 104(4):835-840.

29. Li, X. 2016. Bactericidal mechanism of nanopatterned surfaces. Physical Chemistry Chemical Physics 18(2):1311-1316. 10.1039/C5CP05646B.